Triquinoline vs Fullerene based cycloparaphenylene ionic complexes. Comparison of photoinduced charge-shift reactions.

A. J. Stasyuk,*[a] O. A. Stasyuk,[a] M. Solà*[a] and A. A. Voityuk*[a,b]

a. Institut de Química Computacional and Departament de Química, Universitat de Girona, C/ Maria Aurèlia Capmany 69, 17003 Girona, Spain.

b. Institució Catalana de Recerca i Estudis Avancats (ICREA), 08010 Barcelona, Spain.

Abstract

A triquinoline cationic moiety (TQ•H$^+$) has recently been designed as a novel molecular unit for supramolecular chemistry. In addition to some useful features, TQ•H$^+$ has strong electron acceptor properties which make the molecular cation to be a unique element in nano-chemistry. TQ•H$^+$ is found to form complexes with coronene (COR) and cycloparaphenylene (CPP). In this work, we report a computational study of photoinduced electron transfer (PET) in supramolecular complexes TQ•H$^+$–COR, TQ•H$^+$⊂[12]CPP and (TQ•H$^+$–COR)⊂[12]CPP. The electron transfer rates are estimated by using the semi-classical approach. The calculation results are compared with the data previously obtained for a structurally similar inclusion complex Li$^+$@C$_{60}$⊂[10]CPP. In particular, we find a red solvatochromic shift for charge-shift bands in the TQ•H$^+$-complexes unlike a blue shift showed by Li$^+$@C$_{60}$⊂[10]CPP. This distinction is explored in terms of electronic and structural features of the systems.

Introduction

Synthesis and characterization of structurally well-defined nitrogen-doped graphitic materials suitable for optoelectronic applications is one of the most interesting and challenging topics. Graphitic materials have a variety of outstanding chemical and physical properties that contribute to their growing application.[1-6] Although pristine single-layer graphene has a high charge carrier mobility, its utility in electronic applications is limited by a negligibly small energy gap between the conduction and valence bands. [7-9] Various strategies have been proposed to increase the energy gap.[10] A commonly used approach is structural modification. For instance, the formation of nano-graphenes and graphene bilayers or the curvature of its lattice lead to larger gaps and desired semiconducting properties.[11-12] An alternative strategy is chemical functionalization including hydrogenation and strategic doping with heteroatoms.[13-17] Unfortunately, still the position of the structural defects can hardly be controlled resulting in their random distribution over the material.

Recently Kumagai and co-workers[18] designed and synthesized triquinoline (TQ) to insert the pyridinic-nitrogen defects into graphene sheets. In the trimer, the quinoline units are concatenated at the 2- and 8-positions in a head-to-tail fashion. The suggested protocol consists of a series of Suzuki–Miyaura cross-coupling reactions of 2-chloro substituted derivatives of quinoline accomplished with the inverse-electron-demand hetero-Diels–Alder reaction.[18] It leads to the formation of TQ•TFA (TQ•H$^+$ + CF$_3$COO$^-$) salt and all attempts fail to remove a proton captured at the center of TQ. The proton affinity of TQ is significantly higher than that of the reference proton sponge, 1,8-bis(dimethylamino)naphthalene. Kumagai and co-workers suggested the formation of TQ•H$^+$ based supramolecular entities *via* non-

covalent interactions. They synthesized a plane-to-plane π-complex with coronene, TQ•H$^+$–COR, and an edge-to-plane complex with [12]-cycloparaphenylene, TQ•H$^+$⊂[12]CPP . Two ternary inclusion complexes, (TQ•H$^+$)$_2$⊂[12]CPP and (TQ•H$^+$–COR)⊂[12]CPP, were also identified. The association constants (K$_a$) for 1:1 complexes, TQ•H$^+$–COR and TQ•H$^+$⊂[12]CPP , were determined by ^{1}H NMR titration. Their values, $1.20 \cdot 10^3$ and $1.62 \cdot 10^3$ mol^{-1}·L, indicate a strong interaction between the subunits. As a result, the complexes can also exist in a highly polar environment.[18]

In 2015, Itami and co-workers[19] successfully synthesized and characterized the Li$^+$@C$_{60}$⊂[10]CPP complex with K$_a$ = $4.78 \cdot 10^4$ mol^{-1}·L in dichloromethane. The electrochemical and spectroscopic measurements revealed a strong charge transfer interaction between [10]CPP and Li$^+$@C$_{60}$. Its charge transfer (CT) absorption band demonstrates a solvent induced blue shift due to destabilization of the charge-separated state by polar medium.[20] Since this complex is structurally similar to TQ•H$^+$⊂[12]CPP, one can expect that TQ•H$^+$⊂[12]CPP and other TQ•H$^+$ based complexes can also exhibit photoinduced electron transfer (PET) properties. We note that presumably diquinoline and substituted triquinolines can be used instead of TQ•H$^+$ as an electron acceptor in complexes with [12]CPP. In this context, the resemblance and distinctions in the photochemical behavior of TQ•H$^+$ and Li$^+$@C$_{60}$ are of interest.

Herein, we report a comprehensive computational study PET in the binary and ternary inclusion complexes of TQ•H$^+$.

Results

Structure and ground state properties

The geometries of TQ•H$^+$⊂[12]CPP and Li$^+$@C$_{60}$⊂[10]CPP (Figure 1) were optimized at the B3LYP(D3)/def2-SVP theory level. The vertical electron affinity, the formation energy of the complexes as well as their excitation energies were computed with the CAM-B3LYP(D3)/def2-TZVP scheme.[21-25] The obtained HOMO/LUMO energies of TQ•H$^+$ (-10.35eV/-5.04eV) are comparable with those of Li$^+$@C$_{60}$ (-10.86eV/-5.97eV).
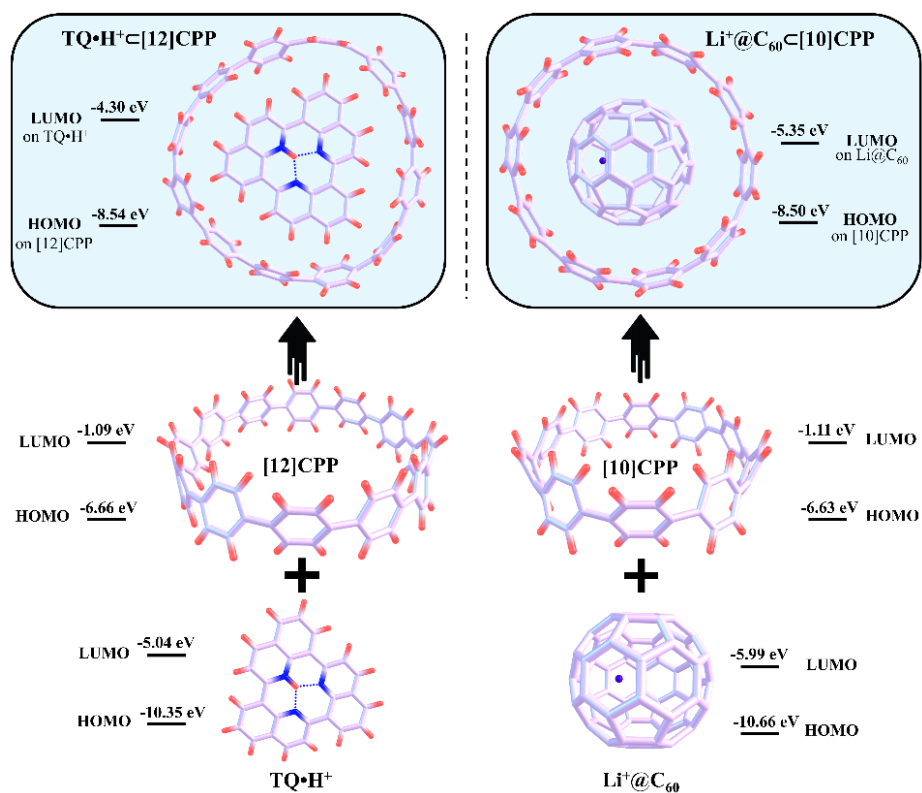
Figure 1. HOMO and LUMO energies, and their localization in TQ•H$^+$⊂[12]CPP, Li$^+$@C$_{60}$⊂[10]CPP and their subunits [12]CPP, [10]CPP, TQ•H$^+$, and Li$^+$@C$_{60}$.

As seen from Figure 1, the formation of the complexes affects dramatically the orbital energies. The HOMOs in both complexes are localized on the CPP moiety and their energies decrease by nearly 2 eV. The changes can be rationalized by the electrostatic potential on CPP caused by inclusion of a positively charged fragment. LUMOs localized on TQ•H$^+$ and Li$^+$@C$_{60}$ are also affected upon the complex formation. Their energies increase by 0.7 eV by passing from the isolated fragments. In order to understand this trend, let us analyze the charge distribution in the complexes. In the ground state (GS) of both TQ•H$^+$⊂[12]CPP and Li$^+$@C$_{60}$⊂[10]CPP, the positive charge (0.88e and 0.80e) is mainly localized on TQ•H$^+$ and Li$^+$@C$_{60}$, respectively. Obviously, the isolated fragments carry the unit charge. Thus, the increase in LUMO energies is associated with the decreasing positive charge on the subunits. Let us compare now structural characteristics of two complexes with the focus on the included fragments. To this end, we estimated the area occupied inside the CPP and an effective radius of TQ•H$^+$, R$_{eff}$ = 6.54Å, and Li$^+$@C$_{60}$, R$_{eff}$ = 5.16Å. It should be mentioned that the shape of TQ•H$^+$ is not perfectly circlic (see Figure S1). Then we also compared [10]CPP and [12]CPP. The structures of individual molecules have nearly D$_5$h and D$_6$h symmetry and are characterized by alternating zigzag orientation of phenylene units. The strain energy of the molecules caused by distortion of the triphenyl fragment from the optimal alignment decreases with an increase of the number of paraphenylene units. For [10]CPP and [12]CPP, the strain energy calculated at the B3LYP/6-31g(d) level of theory[26,27] is found to be 58.9 kcal/mol and 49.1 kcal/mol, respectively, The diameter of [10]CPP and [12]CPP is 13.87Å and 16.61Å.[27,28] The accessible cavity size is smaller by a double van der Waals radius of the carbon atom and is 10.47 and 13.21 Å for [10]CPP and [12]CPP. Comparing these values with R$_{eff}$ of the included molecules, we argue that the fragments in TQ•H$^+$⊂[12]CPP and Li$^+$@C$_{60}$⊂[10]CPP complexes match perfectly in size. We note that the twist angles

between phenyl rings of CPP changes by complexation. In isolated [10]CPP and [12]CPP, the dihedral angles are quite similar (31-32°). However, in the TQ•H$^+$ complex the dihedral angle values can reach 43°, whereas in Li$^+$@C$_{60}$⊂[10]CPP it is about 30°. Such a difference can be explained by a not fully symmetric shape of triquinoline molecule and the strong CH⋯π interaction resulting in a more pronounced distortion of [12]CPP (Figure S2). There is also variation of the bend angle between the phenyl rings (Figure S3) associated with a transformation of the linear chain into CPP. In isolated [12]CPP, all the values are about 162.5°. In TQ•H$^+$⊂[12]CPP , the bend angles are in the range from 157° to 168°. By contrast, when the Li$^+$@C$_{60}$⊂[10]CPP complex forms, only small changes of the angle (within 1-1.5°) are found. (Figure S3).
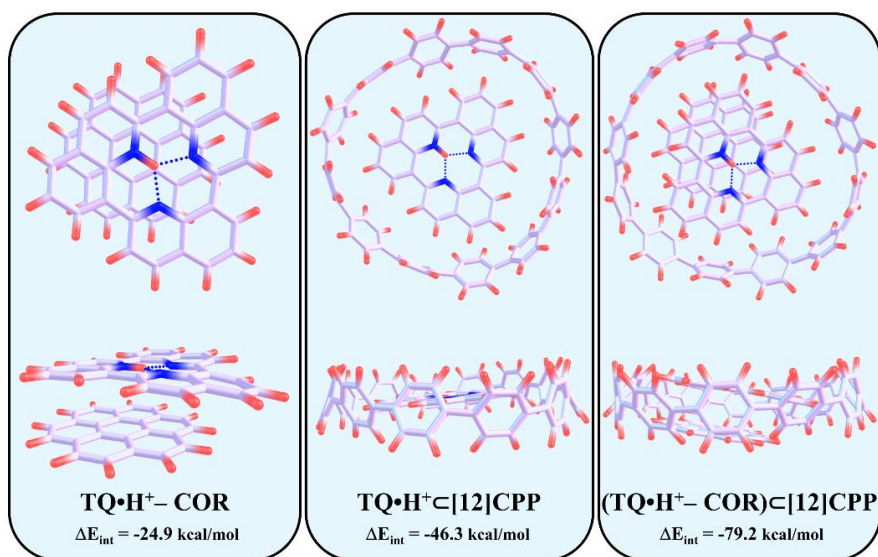
Figure 2. Graphical representations of the studied complexes and their association energies.

The systems TQ•H$^+$−COR, TQ•H$^+$⊂[12]CPP and (TQ•H$^+$−COR)⊂[12]CPP have a large association energy, -24.9, -46.3 and -79.2 kcal/mol, respectively (Figure 2). The computed values correlate well with the experimentally measured association constants.[18] In addition, the association energy for TQ•H$^+$⊂[12]CPP, -46.3 kcal/mol, is in a good agreement with a value of -51.5 kcal/mol computed using the symmetry-adapted perturbation approach.[18]

Singlet excited states

For a more convenient description of the excited states, let us divide the systems into natural subunits (Figure S4, SI). Two fragments TQ•H$^+$ and COR/[12]CPP, will be considered in the binary complexes, and 3 fragments, TQ•H$^+$, COR, and [12]CPP, for the ternary complex. Then, 80 lowest excited states of each complex are described in terms of the exciton localization and charge transfer contributions. Three types of excited states can be identified: locally excited (LE) states, where excitation is mostly localized on a single fragment, CT states with electron density (> 0.9 e) transferred between two fragments (charge transfer > 0.9e); and mixed states with significant contributions of LE and CT. In turn, two types of CT states can be distinguished. 1) Charge shift (*CSh*) states generated by ET from the neutral fragment to TQ•H$^+$. Note that in binary complexes only *CSh* states exist. 2) Charge separation (CS) states resulted from ET between two neutral fragments in ternary complexes. Among considered 80 excited states two types of LE state were selected – lowest LE state located on the TQ•H+ fragment and the LE state with highest

oscillator strength, which corresponds to the most absorptive transition. Each possible type of CT states for studied systems was considered as well.

Among LE states in the complexes, the states localized on TQ•H$^+$ are of the lowest energy, 3.08 – 3.16 eV. The LE states localized on other fragments lie higher by 0.4 – 0.6 eV (Table 1). The CT states generated by electron transfer to TQ•H$^+$ (*CSh$_1$* in TQ•H$^+$–COR and *CSh$_2$* in TQ•H$^+$⊂[12]CPP) are found to be of the lowest-energy. The following CT states are identified in (TQ•H$^+$–COR)⊂[12]CPP complex. The lowest CT state is *CSh$_1$*. It is followed by the *CSh$_2$* and CS states lying by 0.51 and 1.70 eV higher in energy (Table 1). The frontier molecular orbitals representing the LE and CT states are shown in Figures S5-S7.

Table 1. Singlet excitation energy (E$_x$, eV), main singly excited configuration and its weight (W), oscillator strength (f), contribution of charge transfer (CT) and local excitation (X), computed in vacuum (VAC) and dichloromethane (DCM).

	Complexes					
	TQ•H$^+$–COR		TQ•H$^+$⊂[12]CPP		(TQ•H$^+$–COR)⊂[12]CPP	
	VAC	DCM	VAC	DCM	VAC	DCM
	LE$_1$ (TQ•H$^+$)					
E$_x$	3.163	3.218	3.081	3.125	3.113	3.151
Transition (W)	H-2 – L (0.85)	H-2 – L (0.82)	H-5 – L (0.80)	H-3 – L (0.83)	H-5 – L (0.79)	H-5 – L (0.83)
F	0.015	0.031	0.011	0.018	0.011	0.023
X	0.904	0.864	0.982	0.985	0.906	0.874
	Most absorptive transition					
E$_x$	5.470	5.468	4.031	4.101	4.006	4.047
Transition (W)	H-2 – L+4 (0.15)	H-2 – L+5 (0.18)	H – L+5 (0.20)	H-1 – L+1 (0.31)	H-4 – L+1 (0.24)	H-3 – L+1 (0.22)
F	0.344	0.327	2.461	3.489	1.527	2.258
X	0.532	0.418	0.732	0.821	0.718	0.819
Localization	TQ•H$^+$	TQ•H$^+$	[12]CPP	[12]CPP	[12]CPP	[12]CPP
	CSh$_1$ (COR → TQ•H$^+$)					
E$_x$	2.551	2.451	n/a		2.629	2.472
Transition (W)	H – L (0.85)	H – L (0.92)			H-1 – L (0.96)	H-1 – L (0.96)

F	0.007	0.013			0.013	0.017
CT	0.91	0.90			0.90	0.89
	CSh₂ ([12]CPP → TQ•H⁺)					
Eₓ	n/a		2.979	2.759	3.148	2.848
Transition (W)			H − L (0.79)	H − L (0.84)	H − L (0.84)	H − L (0.91)
F			0.001	0.003	< 0.001	0.001
CT			0.99	0.99	1.00	1.00
	CS (COR → [12]CPP)					
Eₓ	n/a		n/a		4.327	3.724
Transition (W)					H-1 − L+1 (0.85)	H-1 − L+1 (0.76)
F					0.006	0.024
CT					0.98	0.93

Solvent effects

To estimate the effect of polar environment on electronic excitations, a well-proven COSMO-like model[29-32] with dichloromethane (DCM) as the solvent was applied. The GS solvation energies are calculated to be -1.76, -1.95, and -2.09 eV for TQ•H⁺–COR, TQ•H⁺⊂[12]CPP and (TQ•H⁺–COR)⊂[12]CPP. Since the complexes carry a positive charge, they interact strongly with the polar medium. The solvent effects are known to be usually small for LE states and quite strong for CT states.[33,34] In the considered systems, however, the estimated changes in solvation energies by passing from GS to CT states are relatively modest. This is because of the ability of the fragments to delocalize the charge. Calculation shows that the difference in dipole moments between CT and GS states are about 14-15 D, whereas it is only 5-6 D for the LE states (for details see Table S1, SI). In DCM, the LE states are higher in energy than *CSh* states, and thus they can be decay efficiently by ET between the fragments. The CS states generated in (TQ•H⁺–COR)⊂[12]CPP by ET between COR and [12]CPP unit remain, however, higher than the LE state when passing from the gas phase to DCM solution.

As mentioned above, TQ•H⁺⊂[12]CPP and Li⁺@C₆₀⊂[10]CPP complexes exhibit some similarity in structural and electronic properties. The hypsochromic solvent shift of the *CSh* band found in Li⁺@C₆₀⊂[10]CPP has been attributed to the ability of the subunits to distribute the charge uniformly over the entire fragment.[20] Since [10]CPP is larger than Li⁺@C₆₀, the final state of the ET reaction, Li@C₆₀⊂[10]CPP⁺, has a smaller solvation energy than the initial state Li⁺@C₆₀⊂[10]CPP. In TQ•H⁺⊂[12]CPP however, we observe a bathochromic shift of the *CSh* band. Comparison of molecular

orbitals (MOs) representing the *CSh* states in TQ•H$^+$ and Li$^+$@C$_{60}$ allows us to explain the qualitative difference in the solvent effects. In the [10]CPP, HOMO is distributed almost evenly over the fragment, while in [12]CPP the corresponding orbital is more localized (Figure 3, left panel). In turn, the distinct localization of the orbitals is caused by structural features of the intercalated fragments (e.g. their size and shape) and the CPP units. The corresponding data are considered in the previous section and SI (Figures S2 and S3).
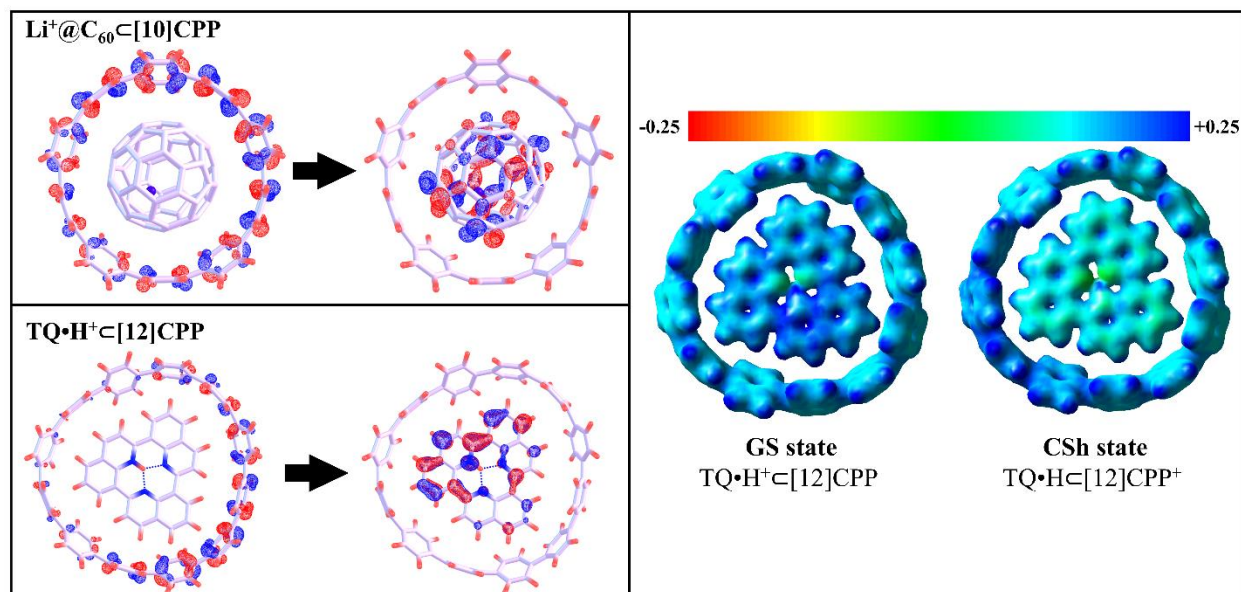
Figure 3. Left panel: Frontier molecular orbitals representing electron transfer from outer CPP to Li$^+$@C$_{60}$ (top) and TQ•H$^+$ (bottom). Right panel: MEP of the GS and *CSh* states of TQ•H$^+$⊂[12]CPP drawn on the isodensity surface of 0.03 e/Å^3.

The solvent effects estimated for vertical electronic transitions within the PCM model are determined by the difference in the electrostatic term of the initial and final states.[35] The molecular electrostatic potential (MEP) of TQ•H$^+$⊂[12]CPP complex in GS and CS is shown in Figure 3. Upon ET from [12]CPP to TQ•H$^+$, the triquinoline subunit becomes almost neutral leading to a decrease of MEP around this fragment. The substantial changes in MEP on [12]CPP are due to inefficient delocalization of the positive charge over the unit related to the large dihedral angles between phenyl groups of [12]CPP in TQ•H$^+$⊂[12]CPP. In contrast, the MEP changes around [10]CPP in the Li$^+$@C$_{60}$⊂[10]CPP complex are small due to strong delocalization of the positive charge.[20] Thus, the different charge delocalization over the CPP units is the crucial factor determining the opposite solvatochromic shift in Li$^+$@C$_{60}$⊂[10]CPP and TQ•H$^+$⊂[12]CPP.

Electron transfer rates

The CT excitations in the complexes are characterized by a weak oscillator strength and therefore cannot be effectively populated by light absorption. However, they can be generated by decay of the lowest LE states. The semi-classical method proposed by Jortner et al.[36,37] was used to compute the electron transfer rates, k_{ET} (for details see SI). In this theory, intramolecular relaxation is described by an effective vibrational mode. The ET rate is controlled by four parameters: electronic coupling V of the initial and final

states, the solvation reorganization energy λ_s, the reaction free energy ΔG_0, and the effective Huang-Rhys factor S_{eff} (for details see SI). The computed parameters and ET rates k_{ET} in DCM are listed in Table 2.

Table 2. ET parameters and the ET rate for charge shift reactions in TQ•H^{+}–COR, TQ•H^{+}⊂[12]CPP and (TQ•H^{+}–COR)⊂[12]CPP in DCM.

Complex	Type	$\Delta G_0^{[a]}$, eV	$|V|$, eV	Reorg. energy, eV		$S_{eff},$[b]	k_{ET}, s[-1]
				λ_i	λ_s		
TQ•H^{+}–COR	LE$_1$→CSh_1	-0.767	4.12·10[-2]	0.146	0.292	1.472	8.11·10[12]
TQ•H^{+}⊂[12]CPP	LE$_1$→CSh_2	-0.366	8.76·10[-4]	0.274	0.377	1.900	2.34·10[10]
(TQ•H^{+}–COR)⊂[12]CPP	LE$_1$→CSh_1	-0.679	4.27·10[-2]	0.170	0.247	1.245	1.28·10[13]
	LE$_1$→CSh_2	-0.303	1.32·10[-3]	0.325	0.294	1.482	5.92·10[10]

[a] Free energy difference between LE$_1$ and *CSh* states in DCM. [b] Effective Huang-Rhys factor $S_{eff} = \lambda_i / \hbar\omega_{eff}$, where $\hbar\omega_{eff}$ is set to $1600\ cm^{-1}$.

The PET in TQ•H^{+}–COR and (TQ•H^{+}–COR)⊂[12]CPP with electron transfer from COR to TQ•H^{+} takes place in the inverted Marcus region ($|\Delta G_0| > \lambda$). These processes can be assigned as ultrafast ET reactions occurring in subpicosecond time scale. In contrast, electron transfer from [12]CPP to TQ•H^{+} to form *CSh_2* in TQ•H^{+}⊂[12]CPP and (TQ•H^{+}–COR)⊂[12]CPP occurs in normal Marcus region ($|\Delta G_0| < \lambda$) on the picosecond time scale with characteristic lifetimes 43 and 17 ps.

The rate of PET in large systems is usually computed using vertical excitation energies. It means that the effect of the structural relaxation of LE states is neglected. To estimate this effect let us consider photoinduced charge shift corresponding to electron transfer from COR to TQ•H^{+} in the TQ•H^{+}–COR complex. The lowest LE state of this system is localized on the TQ•H^{+} fragment. According to our computational results, the structural relaxation of this state leads to a notable planarization of triquinoline fragment (Figure S8) associated with a higher extent of electron density delocalization (Figure S5). The ET simulation using the relaxed geometry shows that the energy of the LE state changes rather significant: E_{LE1} (GS)= 3.22 eV, whereas E_{LE1}(relax) = 2.88 eV. Observed LE energy decreasing by 0.34 eV is associated with large geometrical reorganization. A comparable difference is found for the energy of the *CSh_1* state: E_{CSh1} (GS) = 2.45 eV and E_{CSh1} (relax)= 2.19 eV. Therefore, owing to the structural relaxation of the LE state, ΔG of the charge-shift reaction LE$_1$→CSh_1 changes by about 0.08 eV (for details see Table S4, SI). It is worth noting that some changes are also found in the internal reorganization energies, while solvent reorganization energies remain almost unchanged. Now the estimated rate constant of electron transfer from COR to TQ•H^{+} is nearly twice higher than it was before, $k_{ET}(relax)$= 1.47·10[13] s^{-1} *vs.* $k_{ET}(GS)$ =8.11·10[12] s^{-1}. Thus, the structural relaxation may have a pronounced effect on estimating the ET rate even for relatively large systems.

Conclusions

The photoinduced charge transfer in TQ•H^{+}–COR, TQ•H^{+}⊂[12]CPP, and (TQ•H^{+}–COR)⊂[12]CPP complexes has been studied in detail using TD-DFT calculation. In these complexes, the lowest-lying

excited states correspond to charge shift between the subunits. It has been found that the ET reaction between TQ•H$^+$ and COR occurs in the inverted Marcus region, whereas the charge shift between TQ•H$^+$ and [12]CPP takes place on the nanosecond time scale in the normal Marcus region. In contrast to structurally similar Li$^+$@C$_{60}$⊂[10]CPP complex, CS bands in TQ•H$^+$ based complexes exhibit a red solvatochromic shift. This distinction is mainly caused by non-symmetrical structure of TQ•H$^+$⊂[12]CPP and higher degree of charge localization in TQ•H$^+$ as compared to Li$^+$@C$_{60}$.

Methods

General.
Geometry optimizations were performed using the hybrid B3LYP[21-23] functional with Ahlrichs' Def2-SVP basis set.[25]. Electronic structures calculations, interaction energies of the complexes, electron affinity and vertical excitation energies were calculated using TDA formalism[38] with the range-separated functional from Handy and coworkers' CAM-B3LYP[24] using Gaussian 16 (rev. A03)[39] and Ahlrichs' Def2-SVP or Def2-TZVP triple-ξ quality basis set.[25,40] The empirical Grimme D3 dispersion correction[41] with zero-damping was employed. To visualize molecular structures and frontier molecular orbitals, we used the program Chemcraft 1.8.[42]

Analysis of excited states.
The quantitative analysis of exciton delocalization and charge transfer in the donor-acceptor complexes was carried out using a tool suggested recently by Plasser et al.[43,44] A key quantity is the parameter Ω:

$$\Omega(A,B) = \frac{1}{2} \sum_{\alpha \in A, \beta \in B} \left[\left(SP^{0i} \right)_{\alpha\beta} \left(P^{0i}S \right)_{\alpha\beta} + P^{0i}_{\alpha\beta} \left(SP^{0i}S \right)_{\alpha\beta} \right] \tag{1}$$

$$X(F_i) = \sum_{A \in F_i} \Omega(A,A) \tag{2}$$

$$\Delta q(CT^{F_i \to F_j}) = \sum_{A \in F_i, B \in F_j} \Omega(A,B) + \Omega(B,A) \tag{3}$$

$$\Delta q(CS^{F_i \to F_j}) = \sum_{A \in F_i, B \in F_j} \Omega(A,B) - \Omega(B,A) \tag{4}$$

where A and B are atoms, F_i and F_j are fragments, α and β are atomic orbitals, $\mathbf{P}^{0i}$ is the transition density matrix for the $\psi_0 \to \psi_i$ excitation, and S is the overlap matrix. X(F$_i$) is the extent of exciton localization on the fragment F$_i$. $\Delta q(CT^{F_i \to F_j})$ is the total amount of the electron density transferred between fragments F$_i$ and F$_j$ in the $\psi_0 \to \psi_i$ excitation. $\Delta q(CS^{F_i \to F_j})$) is a measure of the charge separation between fragments F$_i$ and F$_j$. Note that in the situation when charge transfer $\left(F_i \to F_j \right)$ is equal to the back transfer $\left(F_j \to F_i \right)$ there is no charge separation between the fragments and $CS^{F_i \to F_j}$ is equal to zero.

Solvent Effects.

The equilibrium solvation energy E_S^{eq} in a medium with dielectric constant ε was estimated using a COSMO-like polarizable continuum model (CPCM) in the monopole approximation.[29]

$$E_S^{eq}(Q,\varepsilon) = -\frac{1}{2}f(\varepsilon)Q^+DQ \quad ,$$

$$(5)$$

where $f(\varepsilon)$ is the dielectric scaling factor, $f(\varepsilon)=(\varepsilon-1)/\varepsilon$, **Q** is the vector of n atomic charges in the molecular system, and **D** is the n x n symmetric matrix determined by the shape of the boundary surface between solute and solvent; **D=B$^+$A^{-1}B**, where the m x m matrix **A** describes electrostatic interaction between m surface charges and the m x n **B** matrix describes the interaction of the surface charges with n atomic charges of the solute. Atomic charges in the excited state ψ_i, were calculated using Eqs. 1-4.

Electron transfer rates.

The rate of the nonadiabatic ET, k_{ET}, can be expressed in terms of the electronic coupling squared, V^2, and the Franck-Condon Weighted Density of states (FCWD):

$$k_{ET} = \frac{2\pi}{\hbar^2}V^2 \, (FCWD) \qquad (6)$$

that accounts for the overlap of vibrational states of donor and acceptor and can be approximately estimated using the classical Marcus equation:[45]

$$(FCWD) = (4\pi\lambda kT)^{-1/2} \cdot exp\left[-(\Delta G^0 + \lambda)^2 \big/ 4\lambda kT\right] \qquad (7)$$

where λ is the reorganization energy and ΔG^0 is the standard Gibbs energy change of the process. The fragment charge difference (FCD)[46,47] method was employed to calculate the electronic couplings in this work.

The Marcus expression is derived for the high-temperature condition, $\hbar\omega_l \ll kT$, for all vibrational modes l. In the semi-classical description of electron transfer (ET),[36,37] includes the effect of the quantum vibrational modes in an effective way, the solvent (low frequency) modes are treated classically, while a single high-frequency intramolecular mode $\omega_i, \hbar\omega_i \gg kT$, is described quantum mechanically. Because ET occurs normally from the lowest vibrational level of the initial state, the rate k can be expressed as a sum over all channels connecting the initial state with the vibrational quantum number n = 0 to manifold vibrational levels of the final state,

$$k = \sum_{n=0}^{\infty} k_{0 \to n} \text{ , where } k_{0 \to n} = \frac{2\pi}{\hbar} V_{0 \to n}^2 \frac{1}{\sqrt{4\pi\lambda_s kT}} \exp\left[-\frac{\left(\Delta G + v\hbar\omega_i + \lambda_s \right)^2}{4\lambda_s kT} \right], \text{with}$$

$$V_{0 \to n}^2 = V^2 \frac{S^n}{n!} \exp(-S) \tag{8}$$

An effective value of the Huang-Rhys factor S is estimated from the internal reorganization energy λ_i, $S = \lambda_i / \hbar\omega_i$

As seen, an additional parameter (as compared to the Marcus equation) enters the semi-classical expression- the frequency ω_i of an vibrational mode that effectively describes the nuclear intramolecular relaxation following the ET. Typically, in organic systems (including fullerene derivatives) the main contribution to the internal reorganization energy is due to stretching of C=C bonds (the corresponding frequencies are found to be in the range 1400-1800 cm^{-1}). Thus the effective frequency can be set to be 1600 cm^{-1}. It was shown that changing the parameter ω_i within a reasonable range does not lead to significant changes of the computed ET rate.[48]

The reorganization energy is usually divided into two parts, $\lambda = \lambda_i + \lambda_s$, including the internal and solvent terms. The internal reorganization energy λ_i for **COR** $\to$ **TQ•H$^+$** ET corresponds to the energy of structural change when denoted fragments going from initial-state geometries (neutral and cationic for **COR** and **TQ•H$^+$** correspondingly) to charge-transferred-state geometries (cation and neutral for **COR** and **TQ•H$^+$** units, respectively). The λ_i for **[12]CPP** $\to$ **TQ•H$^+$** and **COR** $\to$ **[12]CPP** CT was calculated in the same manner. Solvent reorganization energy corresponds to the energy necessary to move solvent molecules from the position they occupy in the GS to the location they have in the CT state but without charge transfer having occurred. The λ_s for particular CT states were computed as a difference between equilibrium and non-equilibrium solvation energies.

Interaction energies were calculated directly from electronic energies of particular complex and the electronic energies of individual fragments from which this object consists. For **TQ•H$^+$–COR** complex interaction energy can be expressed as follows:

$$\Delta E_{\text{int}} = E_{TQ\cdot H^+ - COR} - (E_{TQ\cdot H^+} + E_{COR}) \tag{9}$$

Ackcknowledgment

References

(1) K. Dirian, M. Á. Herranz, G. Katsukis, J. Malig, L. Rodríguez-Pérez, C. Romero-Nieto, V. Strauss, N. Martín, D. M. Guldi, *Chem. Sci.* **2013,** *4*, 4335-4353.

(2) S. Wu, R. Ge, M. Lu, R. Xu, Z. Zhang, *Nano Energy* **2015,** *15*, 379-405.

(3) G. Bottari, M. Á. Herranz, L. Wibmer, M. Volland, L. Rodríguez-Pérez, D. M. Guldi, A. Hirsch, N. Martín, F. D'Souza, T. Torres, *Chem. Soc. Rev.* **2017,** *46*, 4464-4500.

(4) N. Martín, T. Da Ros, J.-F. Nierengarten, *J. Mat. Chem. B* **2017,** *5*, 6425-6427.

(5) P. Pal, B. Das, P. Dadhich, A. Achar, S. Dhara, *J. Mat. Chem. B* **2017,** *5*, 6645-6656.

(6) Y. Hou, M. Qiu, M. G. Kim, P. Liu, G. Nam, T. Zhang, X. Zhuang, B. Yang, J. Cho, M. Chen, C. Yuan, L. Lei, X. Feng, *Nat. Commun.* **2019,** *10*, 1392.

(7) M. Y. Han, B. Özyilmaz, Y. Zhang, P. Kim, Energy band-gap engineering of graphene nanoribbons. *Phys. Rev. Lett.* **2007,** *98*, 206805.

(8) A. H. Castro Neto, F. Guinea, N. M. R. Peres, K. S. Novoselov, A. K. Geim, *Rev. Mod. Phys.* **2009,** *81*, 109-162.

(9) F. Schwierz, *Nat. Nanotechnol.* **2010,** *5*, 487-496.

(10) A. Narita, X.-Y. Wang, X. Feng, K. Müllen, *Chem. Soc. Rev.* **2015,** *44*, 6616-6643.

(11) P. J. Evans, J. Ouyang, L. Favereau, J. Crassous, I. Fernández, J. Perles, N. Martín, *Angew. Chem. Int. Ed.* **2018,** *57*, 6774-6779.

(12) J. M. Fernández-García, P. J. Evans, S. Medina Rivero, I. Fernández, D. García-Fresnadillo, J. Perles, J. Casado, N. Martín, *J. Am. Chem. Soc.* **2018,** *140*, 17188-17196.

(13) J. Son, S. Lee, S. J. Kim, B. C. Park, H.-K. Lee, S. Kim, J. H. Kim, B. H. Hong, J. Hong, *Nat. Commun.* **2016,** *7*, 13261.

(14) U. Bangert, W. Pierce, D. M. Kepaptsoglou, Q. Ramasse, R. Zan, M. H. Gass, J. A. Van den Berg, C. B. Boothroyd, J. Amani, H. Hofsäss, *Nano Lett.* **2013,** *13*, 4902-4907.

(15) J. H. Warner, Y.-C. Lin, K. He, M. Koshino, K. Suenaga, *ACS Nano* **2014,** *8*, 11806-11815.

(16) Y. Wang, J. Mao, X. Meng, L. Yu, D. Deng, X. Bao, *Chem. Rev.* **2019,** *119*, 1806-1854.

(17) Y.-C. Lin, P.-Y. Teng, C.-H. Yeh, M. Koshino, P.-W. Chiu, K. Suenaga, *Nano Lett.* **2015,** *15*, 7408-7413.

(18) S. Adachi, M. Shibasaki, N. Kumagai, *Nat. Commun.* **2019,** *10*, 3820.

(19) H. Ueno, T. Nishihara, Y. Segawa, K. Itami, *Angew. Chem. Int. Ed.* **2015,** *54*, 3707-3711.

(20) A. J. Stasyuk, O. A. Stasyuk, M. Solà, A. A. Voityuk, *Chem. Commun.* **2019,** *55*, 11195-11198.

(21) C. Lee, W. Yang, R. G. Parr, *Phys. Rev. B* **1988,** *37*, 785-789.

(22) A. D. Becke, *J. Chem. Phys.* **1993,** *98*, 1372-1377.

(23) P. J. Stephens, F. J. Devlin, C. F. Chabalowski, M. J. Frisch, *J. Phys. Chem.* **1994,** *98*, 11623-11627.

(24) T. Yanai, D. P. Tew, N. C. Handy, *Chem. Phys. Lett.* **2004,** *393*, 51-57.

(25) K. Eichkorn, F. Weigend, O. Treutler, R. Ahlrichs, *Theor. Chem. Acc.* **1997,** *97*, 119-124.

(26) T. Iwamoto, Y. Watanabe, Y. Sakamoto, T. Suzuki, S. Yamago, *J. Am. Chem. Soc.* **2011**, *133*, 8354-8361.

(27) S.M. Bachrach, D. Stück, *J. Org. Chem.* **2010**, *75*, 6595-6604.

(28) Y. Segawa, H. Omachi, K. Itami, *Org. Lett.* **2010**, *12*, 2262-2265.

(29) J. Tomasi, B. Mennucci, R. Cammi, *Chem. Rev.* **2005,** *105*, 2999-3094.

(30) A. J. Stasyuk, O. A. Stasyuk, M. Solà, A. A. Voityuk, *Chem. Eur. J.* **2018,** *24*, 13020-13025.

(31) A. J. Stasyuk, O. A. Stasyuk, M. Solà, A. A. Voityuk, *Chem. Eur. J.* **2019,** *25*, 2577-2585.

(32) M. Izquierdo, B. Platzer, A. J. Stasyuk, O. A. Stasyuk, A. A. Voityuk, S. Cuesta, M. Solà, D. M. Guldi, N. Martín, *Angew. Chem. Int. Ed.* **2019,** *131*, 7006-7011.

(33) G. J. Kavarnos, N. J. Turro, *Chem. Rev.* **1986,** *86*, 401-449.

(34) B. Bagchi, *Annu. Rev. Phys. Chem.* **1989,** *40*, 115-141.

(35) B. Mennucci, *Wiley Interdiscip. Rev.: Comput. Mol. Sci.* **2012,** *2*, 386-404.

(36) J. Ulstrup, J. Jortner, *J. Chem. Phys.* **1975,** *63*, 4358-4368.

(37) J. Jortner, *J. Chem. Phys.* **1976,** *64*, 4860-4867.

(38) S. Hirata, M. Head-Gordon, Chem. Phys. Lett. **1999**, *314*, 291-299.

(39) Gaussian 16, Revision A.03 (Wallingford CT, 2016). Full citation see in SI.

(40) F. Weigend, Phys. Chem. Chem. Phys. **2006**, *8*, 1057-1065.

(41) S. Grimme, J. Antony, S. Ehrlich, S. Krieg, J. Chem. Phys. **2010**, *132*, 154104

(42) G. A. Zhurko, Chemcraft 1.80 (build 523b) - graphical program for visualization of quantum chemistry computations. (https://chemcraftprog.com).

(43) F. Plasser, H. Lischka, *J. Chem. Theory Comput.* **2012**, *8*, 2777-2789.

(44) F. Plasser, S. A. Bäppler, M. Wormit, A. Dreuw, *J. Chem. Phys.* **2014**, *141*, 024107.

(45) R. A. Marcus, N. Sutin, *Biochim. Biophys. Acta, Rev. Bioenerg.* **1985,** *811,* 265-322.

(46) A. A. Voityuk, N. Rösch, *J. Chem. Phys.* **2002,** *117,* 5607-5616.

(47) A. A. Voityuk, *Phys. Chem. Chem. Phys.* **2012,** *14,* 13789-13793.

(48) T. Liu, A. Troisi, J. Phys. Chem. C **2011**, *115*, 2406-2415